

Time-Domain Finite Element Models of Electrochemistry in Intracochlear Electrodes

Andrian Sue, *Student Member, IEEE*, Phillip Tran, *Student Member, IEEE*,
Paul Wong, *Student Member, IEEE*, Qing Li, and Paul Carter

Abstract—Most neural prostheses feature metallic electrodes to act as an interface between the device and the physiological tissue. When charge is injected through these electrodes, potentially harmful reactions may result. Others have developed finite element models to evaluate the performance of stimulating electrodes *in vivo*. Few however, model an electrode-electrolyte interface, and many do not address electrode corrosion and safety concerns with respect to irreversible reactions. In this work, we successfully develop a time domain finite element model of cochlear implant electrodes that incorporate oxygen reduction and platinum oxidation reactions. We find that when electrodes are stimulated with current pulses (0.5 mA, 25 μ s), faradaic reactions may cause an increase in the peripheral enhancement of the current density.

I. INTRODUCTION

Cochlear implants and other neural prostheses utilize metallic electrodes as a means of interfacing with excitable tissues of the body. Most contemporary cochlear implant arrays feature half-banded or hemicylindrical electrodes on a silicone carrier. These include the Contour Advance and CI422 arrays manufactured by Cochlear Ltd. These arrays are implanted into the inner ear and enable electrical charge delivery to nerve fibers. Inherent to charge injection with these electrodes is the occurrence of electrochemical reactions that may be detrimental to the operation of the prosthesis. These reactions may cause corrosion of the electrode surface and produce harmful by-products that facilitate tissue damage. To date, numerous studies have been conducted to investigate the damage caused by stimulating electrodes and develop guidelines to avoid such damage [1]-[3]. Much of the electrode safety knowledge is based on empirical data published in such literature.

There has been increasing interest in this area due to the development of novel neural prostheses requiring smaller electrodes with more complex geometries. Finite element models have been used to help predict the performance of stimulating electrodes *in vivo*. Most of these aimed to model the activation of neural tissue, however until recently, many have not added the effects of the electrode-electrolyte interface. Of the published cochlear implant models, only

simplistic representations of the electrochemistry have been modeled and the actual electrochemical consequences are neglected to date [4], [5]. These studies attempted to account for the electrical characteristics imparted by these electrochemical processes because they may significantly affect clinical measures such as impedance. Cantrell *et al.* incorporated an electrode-electrolyte interface into an electrical model of disc and needle electrodes [6]. Their study was based purely in the frequency domain and used rather general parameters to define their faradaic reaction kinetics, assuming a symmetrical current-overpotential relationship. Behrend *et al.* produced a study of edge effects on disc electrodes in the time-domain, but assumed the electrode-electrolyte interface was a simple capacitor and hence, modeled the electrode as being ideally polarizable [7].

These past works have examined the effect of the electrode-electrolyte interface, without explicitly considering the reactions that provide the applied electrical phenomena. This study uses finite element methods to analyze two reactions known to occur on cochlear implant electrodes. Their distribution and rates on two different sized electrodes will be discussed. Such an analysis may provide valuable insight to the future design of intracochlear electrodes.

II. METHODS

A. Geometry Construction

To mimic an intracochlear electrode array, a hemicylindrical electrode on cylindrical silicone carrier was modeled in the finite element package, COMSOL v4.3a (COMSOL, Burlington, MA). The electrode and carrier were centered in a larger cylinder that represented the perilymph of the cochlea. The size of the electrodes was varied by changing the electrode length, as defined in Fig. 1. The confined space of the cochlea restricts changes to many other electrode dimensions. To highlight the sensitivity of the results to the electrode size, electrodes with lengths of 0.10 mm and 0.30 mm were chosen. A length of 0.30 mm is typical for an intracochlear electrode. Electrodes will be identified by their length for the remainder of this paper.

Electrical conductivity (σ) and relative permittivity (ϵ_r) values used for platinum ($\sigma = 94.35 \times 10^5$ S/m, $\epsilon_r = 1$), silicone ($\sigma = 10^{-14}$ S/m, $\epsilon_r = 4.2$) and perilymph ($\sigma = 1.42$ S/m, $\epsilon_r = 78$) were consistent with those used in the previous studies [6]. Physiological saline is similar in composition to the perilymph in the scala tympani, so it was assumed that the electrical properties of both fluids are also similar.

Research supported by the Australian Research Council (ARC) and Cochlear Ltd. A. Sue, P. Tran & P. Wong are recipients of Australian Postgraduate Awards (APAs).

All authors are with the School of Aerospace, Mechanical and Mechatronic Engineering, Faculty of Engineering and IT, University of Sydney, NSW 2006 Australia. (Tel.: +612-9351-5674; Fax: +612-9351-7060; email: andrian.sue@sydney.edu.au, qing.li@sydney.edu.au)

P. Carter is also a Technology Cluster Leader with Cochlear Ltd., Macquarie University, NSW 2109 Australia. (email: pcarter@cochlear.com)

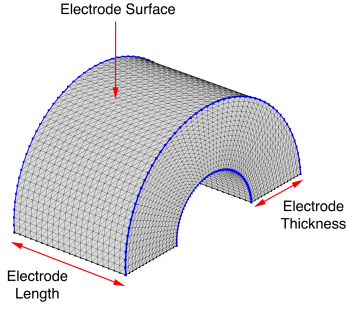


Fig. 1. Electrode domain showing definition of geometrical parameters.

B. Boundary Conditions

All domains in the electric models were solved for electric potential (V) using the electric currents module in COMSOL. To simulate the electrical conditions of an implanted cochlea, the ends of the electrolyte cylinder were grounded ($V = 0$). A current terminal is located at the inner surface of the stimulating electrode, to maintain a constant stimulation current of ± 0.5 mA. Positive and negative terminal current values enabled separate cathodic and anodic models, respectively. Neumann boundary conditions ($\mathbf{n} \cdot \mathbf{J} = 0$) are assumed for all external surfaces of the electrolyte and the boundaries between the electrode and carrier, apart from those grounded. $\mathbf{n} \cdot \mathbf{J}$ is current density normal to the boundary.

The electrode impedance imparted by the electrode-electrolyte interface was implemented using the Robin boundary condition, similar to that described in recent literature [6], [8]. The following subsections describe the impedances that were used to model the electrochemistry. These separate impedances are combined in parallel and incorporated into the aforementioned boundary condition.

1) *Non-Faradaic Impedance Model:* A constant-phase expression in the frequency domain can be used to model the pseudocapacitive behavior, as shown in (1), where K and β are the constant-phase coefficient and exponent, respectively, ω is the angular frequency ($2\pi f$), and $i = \sqrt{-1}$.

$$Z_{CPA} = K(i\omega)^{-\beta} \quad (1)$$

To apply constant-phase behavior in the time-domain, a technique similar to that used by Sadkowski [9] was employed. Let $s = i\omega$, and apply Ohm's Law in the complex frequency (s) domain.

$$I(s) = \frac{1}{K} s^\beta V(s) \quad (2)$$

For a current step,

$$I(s) = \frac{\Delta I}{s}, \quad (3)$$

and thus,

$$V(s) = \frac{K \Delta I}{s^{\beta+1}}. \quad (4)$$

To determine the voltage response in the time-domain, an inverse Laplace transform was used. Using Ohm's Law in

TABLE I
FARADAIC REACTION PARAMETERS, FROM [11].

Parameter	Shorthand	Value
Anodic Transfer Coefficient	α_a	0.099
Cathodic Transfer Coefficient	α_c	0.378
Exchange Current Density	i_0	9.14×10^{-3} A/m ²
Electrons	n	2
Temperature	T	298 K

the time-domain, the impedance may be extracted, as in (5), where t is time in seconds and Γ is the gamma function. Values for K and β have been empirically determined in published literature [10]. In this model, $\beta = 0.91$ and $K = 1.57 \Omega \text{m}^2 \text{s}^{-\beta}$.

$$Z_{CPA,t} = \frac{K}{\Gamma(\beta + 1)t^\beta} \quad (5)$$

2) *Faradaic Impedance Model:* The Butler-Volmer form of the current-overpotential equation was utilized with Ohm's Law to provide a faradaic or charge transfer resistance, shown in (6). This assumes that the electrode is being operated around its equilibrium potential and the kinetics of the faradaic reactions are not mass-transport limited.

$$R_{CT} = \frac{\eta}{i_0 \{e^{-\alpha_c n f \eta} - e^{\alpha_a n f \eta}\}} \quad (6)$$

In (6), f is $\frac{F}{RT}$, where F is Faraday's constant, R is the universal gas constant and T is the temperature in Kelvin. The other parameters are defined in Table I. The kinetic parameters were determined from potentiodynamic control experiments by Richardot *et al.* [10] for 1.3 cm² area platinum electrodes in phosphate buffered saline (PBS). The overpotential (η) was defined at each node on the electrode surface as the electric potential difference between the electrode domain and the electrolyte domain.

C. Solver

The created geometrical domains were discretized into mixed hexahedral and tetrahedral quadratic elements. The final models had 7381 nodes on the surface of each electrode geometry. Models were solved in the COMSOL environment, using the PARDISO direct linear solver coupled with a damped Newton nonlinear solver. Time-steps were chosen according to a backward differentiation formula (BDF) algorithm over a 25 μs period, to resemble a constant current pulse used in a cochlear implant. Electric potential and current density data were then exported into MATLAB (The MathWorks, Natick, MA) for post-processing.

III. RESULTS

To quantify and analyze the current density distribution on the electrode surface, a normalized standard deviation measured was adopted, similar to that described by Behrend *et al.* [7]. Given the constant current supplied to the electrode domain, it is expected that the mean surface current density should be equal to the geometric current density j_{avg} , given by (7), where I is the current (± 0.5 mA) and A is the geometric area of the electrode surface in m².

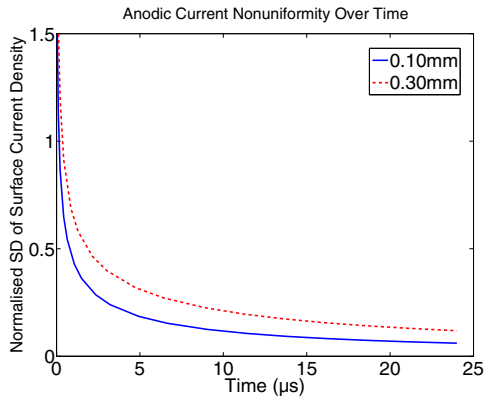


Fig. 2. Current non-uniformity as defined by (8) during an anodic current pulse for 0.10 mm and 0.30 mm length electrodes.

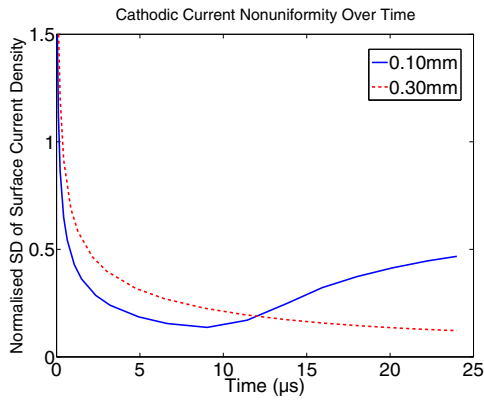


Fig. 3. Current non-uniformity as defined by (8) during a cathodic current pulse for 0.10 mm and 0.30 mm length electrodes.

Hence, the standard deviation of the surface current density values calculated by the model may be normalized by the geometric or mean current density as in (8), giving a result that is comparable across different electrode geometries, where j_n is the nodal current density and N is number of electrode surface nodes.

$$j_{avg} = \frac{I}{A} \quad (7)$$

$$\sigma_{norm} = \frac{1}{j_{avg}} \sqrt{\frac{1}{N} \sum_{n=1}^N (j_n - \bar{j})^2} \quad (8)$$

Fig. 2 and Fig. 3 show the changes in the surface current non-uniformity, or σ_{norm} , over anodic and cathodic pulses, respectively. In the anodic case, the initial distribution of current for both 0.10 mm and 0.30 mm electrodes are highly non-uniform and heavily biased towards the edges and vertices of the electrodes, however this falls rapidly and charge is redistributed resulting in a relatively uniform distribution by the end of the pulse. The larger 0.30 mm electrode exhibits a lower rate of charge redistribution when compared to the 0.10 mm electrode. The σ_{norm} values for the 0.10 mm and 0.30 mm electrode at the end of the anodic pulse are 0.061 and 0.119, respectively.

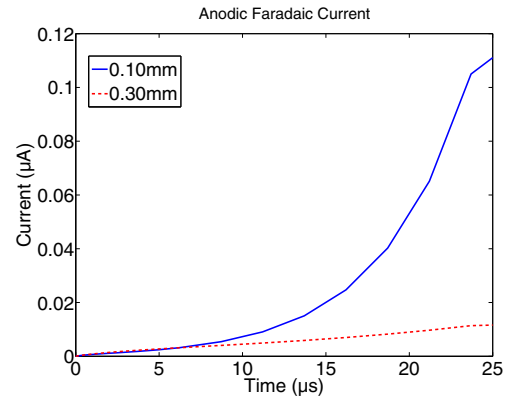


Fig. 4. Faradaic currents generated over a 0.5 mA anodic current pulse for 0.10 mm and 0.30 mm length electrodes.

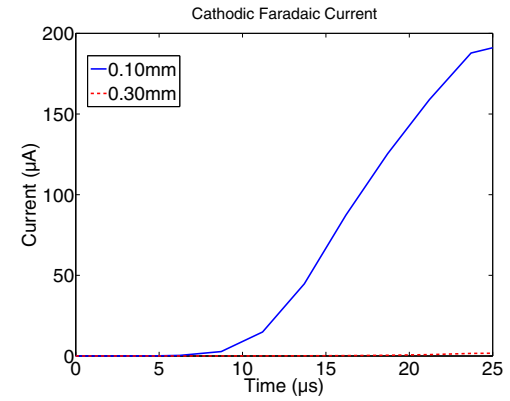


Fig. 5. Faradaic currents generated over a 0.5 mA cathodic current pulse for 0.10 mm and 0.30 mm length electrodes.

The current non-uniformity during a cathodic pulse, shown in Fig. 3, also exhibits rapid charge redistribution to a more uniform current profile. At approximately 9 μs , however, σ_{norm} on the 0.10 mm electrode increases to 0.468 at the end of the pulse. The σ_{norm} on the 0.30 mm electrode behaves similarly to the anodic case, decreasing monotonically to 0.122 at the end of the pulse.

Fig. 4 and Fig. 5 show anodic and cathodic faradaic currents over time, respectively. The maximum faradaic current accounts for 0.022% of the total current for the 0.10 mm electrode and 0.002% for the 0.30 mm electrode. Similarly for the cathodic pulses, the faradaic current reaches 38.2% and 0.340% of total current for 0.10 mm and 0.30 mm electrodes, respectively. If faradaic current density is plotted on the electrode surface (Fig. 6), it is found to be enhanced at the periphery, especially at the corners.

IV. DISCUSSION

For both anodic and cathodic phases, the initial current distribution on the electrodes resembles the primary current distribution for a disc electrode, analytically derived by Newman [11], where the current density is theoretically infinite at the periphery. For the half-banded electrodes modeled in this study, the current density is also found to be high at the

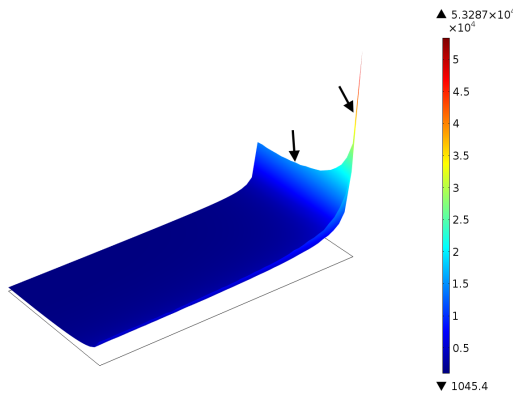


Fig. 6. One corner of the 0.10 mm hemicylindrical electrode surface plane, showing cathodic faradaic current density distribution at peak faradaic current. Current density magnitude is also represented by the magnitude of deformation normal to the base plane (black rectangle). Arrows indicate edge and vertex enhancement of faradaic current. Legend units are A/m².

periphery, but highest at the vertices of the electrode surface, which is not evident in the studies of disc electrodes.

Fig. 2 resembles those presented by Wang *et al.* [12] for ideally polarizable disc electrodes, which suggests minimal faradaic current in the anodic phase for both electrodes. The faradaic current data in Fig. 4 confirms this, although the current rises at a non-linear rate, which may become significant with longer pulse widths. During the cathodic phase (Fig. 5), a marked increase in the faradaic current occurs, especially for the 0.10 mm electrode. Examining Fig. 6, it seems that most of this current tends towards the corners, much like the primary current distribution. This is thought to contribute to the increase in σ_{norm} observed in Fig. 3.

The source for the kinetics parameters used in this model, Richardot *et al.* [10], attributes the anodic and cathodic responses to non-passivating platinum oxide (PtO) formation and dissolved oxygen reduction, respectively. Voltammetry data of platinum electrodes in phosphate-buffered saline provides evidence to support this [13]. The results suggest a large proportion of current is committed to oxygen reduction during cathodic phases, which is consistent with experimental studies of platinum electrodes *in vitro* [14]. This oxygen reduction reaction may result in the production of hydrogen peroxide under conditions where the reaction is not limited by mass transport [15]. Hydrogen peroxide may lower pH levels in the perilymph of the cochlea, contributing to platinum dissolution and potential tissue damage. Future work will seek to optimize the design of smaller electrodes to avoid such behavior.

Previous studies have modeled frequency dependent properties using a Fourier approach [16]. This may be a more flexible approach when studying full biphasic waveforms. The Laplace transform derived for the presented models works well for single current pulses, and spares the added complexity of translating results back to the time domain. It should also be noted that the overpotential-independent forms K and β were used here to reduce the computational load. This was not thought to be of severe consequence as non-linear faradaic processes are thought to dominate

the overall non-linearity of the electrode impedance [10]. Platinum electrodes also exhibit other well-defined faradaic charge transfer processes that are not modeled here, such as platinum dissolution and gas evolution. Modeling these reactions may affect the current distribution at higher overpotentials.

V. CONCLUSION

Finite element methods allow analysis of realistic electrode geometries in neural stimulation applications. The models presented here focus on specific electrochemical aspects of these stimulating electrodes. The results of this study show potential for optimization to avoid peripheral current enhancement, or “edge effects”. More insight may be gained through such models by including reversible faradaic processes, incorporating mass transport of ionic species to and from the electrode surface and studying biphasic stimulation pulses.

REFERENCES

- [1] S. B. Brummer and M. J. Turner, “Electrochemical Considerations for Safe Electrical Stimulation of the Nervous System with Platinum Electrodes,” *IEEE Trans. Biomed. Eng.*, vol. 24, no. 1, pp. 59–63, 1977.
- [2] T. L. Rose and L. S. Robblee, “Electrical stimulation with Pt electrodes. VIII. Electrochemically safe charge injection limits with 0.2 ms pulses (neuronal application),” *IEEE Trans. Biomed. Eng.*, vol. 37, no. 11, pp. 1118–1120, 1990.
- [3] R. V. Shannon, “A model of safe levels for electrical stimulation,” *IEEE Trans. Biomed. Eng.*, vol. 39, no. 4, pp. 424–426, 1992.
- [4] F. J. Vanpoucke, A. J. Zarowski, and S. A. Peeters, “Identification of the impedance model of an implanted cochlear prosthesis from intracochlear potential measurements,” *IEEE Trans. Biomed. Eng.*, vol. 51, no. 12, pp. 2174–2183, 2004.
- [5] W.-D. Lai and C. T. M. Choi, “Incorporating the Electrode-Tissue Interface to Cochlear Implant Models,” *IEEE Trans. Magn.*, vol. 43, no. 4, pp. 1721–1724, 2007.
- [6] D. R. Cantrell, S. Inayat, A. Taflove, R. S. Ruoff, and J. B. Troy, “Incorporation of the electrode-electrolyte interface into finite-element models of metal microelectrodes,” *J. Neural Eng.*, vol. 5, no. 1, pp. 54–67, 2008.
- [7] M. R. Behrend, A. K. Ahuja, and J. D. Weiland, “Dynamic Current Density of the Disk Electrode Double-Layer,” *IEEE Trans. Biomed. Eng.*, vol. 55, no. 3, pp. 1056–1062, 2008.
- [8] S. Joucla and B. Yvert, “Modeling extracellular electrical neural stimulation: From basic understanding to MEA-based applications,” *J. Physiol. Paris*, vol. 106, no. 3, pp. 146–158, 2012.
- [9] A. Sadkowsky, “Time domain responses of constant phase electrodes,” *Electrochim. Acta*, vol. 38, no. 14, pp. 2051–2054, 1993.
- [10] A. Richardot and E. T. McAdams, “Harmonic analysis of low-frequency bioelectrode behavior,” *IEEE Trans. Med. Imag.*, vol. 21, no. 6, pp. 604–612, 2002.
- [11] J. Newman, “Resistance for Flow of Current to a Disk,” *J. Electrochem. Soc.*, vol. 113, no. 5, pp. 501–502, 1966.
- [12] B. Wang and J. D. Weiland, “Reduction of current density at disk electrode periphery by shaping current pulse edges,” in *IEEE-EMBS Annual Meeting Conference Proceedings*, San Diego, CA, USA, 2012.
- [13] E. M. Hudak, J. T. Mortimer, and H. B. Martin, “Platinum for neural stimulation: voltammetry considerations,” *J. Neural Eng.*, vol. 7, no. 2, p. 026005, 2010.
- [14] S. F. Cogan, J. Ehrlich, T. D. Plante, M. D. Gingerich, and D. B. Shire, “Contribution of Oxygen Reduction to Charge Injection on Platinum and Sputtered Iridium Oxide Neural Stimulation Electrodes,” *IEEE Trans. Biomed. Eng.*, vol. 57, no. 9, pp. 2313–2321, 2010.
- [15] D. Pletcher and S. Sotiropoulos, “A study of cathodic oxygen reduction at platinum using microelectrodes,” *J. Electroanal. Chem.*, vol. 356, no. 1, pp. 109–119, 1993.
- [16] C. R. Butson and C. C. McIntyre, “Tissue and electrode capacitance reduce neural activation volumes during deep brain stimulation,” *Clin. Neurophysiol.*, vol. 116, no. 10, pp. 2490–2500, 2005.